HAL
open science

Field-induced mononuclear cobalt(II) single-molecule magnet (SMM) based on a benzothiadiazole-ortho-vanillin ligand †

Nataliya Plyuta, Svitlana Petrusenko, Vladimir N Kokozay, Thomas Cauchy, Francesc Lloret, Miguel Julve, Joan Cano, Narcis Avarvari

To cite this version:

Nataliya Plyuta, Svitlana Petrusenko, Vladimir N Kokozay, Thomas Cauchy, Francesc Lloret, et al.. Field-induced mononuclear cobalt(II) single-molecule magnet (SMM) based on a benzothiadiazole-ortho-vanillin ligand †. Dalton Transactions, 2022, 51 (12), pp.4760-4771. 10.1039/D1DT04274B . hal-03855033

HAL Id: hal-03855033

https://univ-angers.hal.science/hal-03855033v1

Submitted on 16 Nov 2022

HAL is a multi-disciplinary open access archive for the deposit and dissemination of scientific research documents, whether they are published or not. The documents may come from teaching and research institutions in France or abroad, or from public or private research centers.

L'archive ouverte pluridisciplinaire **HAL**, est destinée au dépôt et à la diffusion de documents scientifiques de niveau recherche, publiés ou non, émanant des établissements d'enseignement et de recherche français ou étrangers, des laboratoires publics ou privés.

Field-induced mononuclear cobalt(II) single-molecule magnet (SMM) based on a benzothiadiazole-*ortho*-vanillin ligand†

Nataliya Plyuta,[a,b] Svitlana Petrusenko,[b] Vladimir N. Kokozay,[b] Thomas Cauchy,[a] Francesc Lloret,[c] Miguel Julve,[c] Joan Cano*[c] and Narcis Avarvari*[a]

[a] *Univ Angers, CNRS, MOLTECH-Anjou, SFR MATRIX, F-49000 Angers, France. E-mail: narcis.avarvari@univ-angers.fr*

[b] *Department of Inorganic Chemistry, Taras Shevchenko National University of Kyiv, Volodymyrska str. 64/13, Kyiv 01601, Ukraine*

[c] *Instituto de Ciencia Molecular (ICMol)/Departament de Química Inorgànica, Universitat de València, C/ Catedrático José Beltrán 2, 46980 Paterna (Valencia) (Spain). E-mail: Joan.Cano@uv.es*

†Electronic supplementary information (ESI) available: Figures S1-S15, Tables S1-S9). CCDC reference number 2128849–2128850. For ESI and crystallographic data in CIF or other electronic format see DOI: 10.1039/xxxxx.

Abstract

A unique π-conjugated benzothiadiazole-*ortho*-vanillin ligand (HL), characterized by single crystal X-ray diffraction and DFT calculations, has been prepared by condensation between 4-amino-benzothiadiazole (BTD) and *ortho*-vanillin. Its reaction with cobalt(II) acetate afforded the complex of formula $[CoL_2]\cdot CH_2Cl_2$ (**1**), for which the coordination environment of the cobalt centre is a distorted octahedron and the ligand acts as a monoanionic tridentate *NNO* chelate in its phenolate form. Intermolecular π-π stacking interactions between the π-conjugated BTD units provides an antiferromagnetic coupling pathway, as indicated by the analysis of the dc magnetic measurements of a crystalline sample of complex and supported by DFT type calculations. The static magnetic behaviour of **1** is analysed according to spin-orbit coupling and zero-field splitting models. Remarkably, the complex exhibits slow relaxation of the magnetization under applied magnetic field being thus a new example of field-induced mononuclear single-molecule magnet (SMM).

Introduction

The 2,1,3-benzothiadiazole (BTD) unit occupies a privileged place in the field of organic electronics, since it has been largely used in the composition of precursors for efficient materials as organic light emitting diodes (OLED),[1,2] organic and dye sensitized solar cells,[3,4,5,6] or organic field-effect transistors (OFET),[7,8,9] thanks to its electron acceptor fluorophore properties.[10] Moreover, fluorescent probes,[11,12] polymeric thermometers,[13] and redox switchable donor-acceptor systems[14,15] containing the BTD platform have been reported in the last fifteen years. Interestingly, the BTD fragment takes part in a variety of supramolecular interactions in the solid state, such as non-covalent N⋯S bonding, π-π stacking interactions and hydrogen bonding.[16] It is thus not surprising that BTD has been used over the years as monotopic[17] or ditopic[18,19,20,21] ligand in coordination chemistry due to the presence of the two sp^2 hybridized nitrogen atoms, although the number of reported transition metal complexes remains rather limited. More recently, the introduction of coordinating groups on the benzene ring afforded various functional ligands providing complexes, in which the thiadiazole unit can be involved or not in the coordination to metal centres,[22] such as luminescent coordination polymers with dicarboxylate-BTD derivatives,[23,24,25,26] 4,7-bis(4'-pyridyl)-BTD,[27] or more recently, mononuclear, binuclear and coordination polymers of Zn(II) and Ag(I) within a series of 4,7-bis(pyridyl)-BTD.[28] A very interesting coordination chelating platform, extensively used in the preparation of functional mono- and polynuclear complexes, is the salen type unit which is derived from the condensation of mono- or diamines with salicylaldehyde or *ortho*-vanillin.[29,30,31] However, to the best of our knowledge, the association of a salen platform with BTD has been never reported but once through the luminescent Zn(II) complex obtained by the template condensation of 5,6-diamino-BTD and 4-(hexyloxy)-2-hydroxybenzaldehyde in the presence of zinc(II) acetate.[32] Note that the connection of the salen unit to the benzene ring of BTD at the 5,6-positions in this unique example does not allow the participation of the BTD nitrogen atoms to the chelation.

We report herein the synthesis and characterization, including single crystal X-ray structure and DFT calculations, of the first example of BTD-*o*-vanillin ligand (HL, Scheme 1) together with its neutral cobalt(II) complex showing field-induced single-molecule magnet (SMM) properties. The connection between BTD and *o*-vanillin in position 4 of the BTD benzene ring creates the pre-requisite for a tris-chelation involving the adjacent BTD nitrogen atom, and thus the generation of a quite anisotropic coordination environment.

Results and discussion

Synthesis and characterization of HL

The synthetic procedure involves the preparation of the 4-amino-BTD precursor **3** by the reduction of the nitro compound **2**,[33] obtained by nitration of BTD,[34] followed by condensation of **3** with *o*-vanillin in ethanol to obtain the BTD Schiff base HL in good yield (Scheme 1).

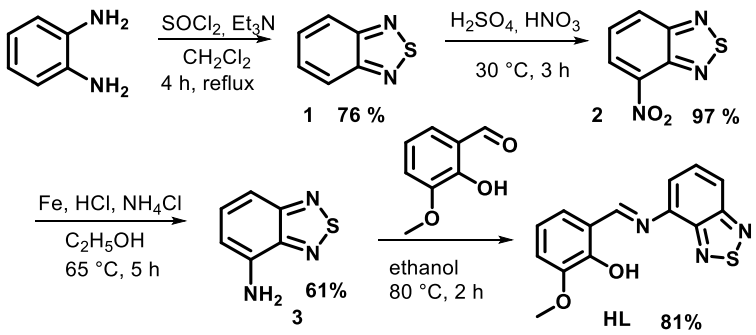

Scheme 1 Synthesis of the BTD Schiff base HL.

Suitable single crystals of HL for X-ray diffraction analysis have been obtained by slow evaporation of methylene chloride/methanol (1:1 v/v) solution. The compound, which crystallized in the centrosymmetric monoclinic space group $P2_1/c$ with one independent molecule in the unit cell (Table S1), shows an *E* conformation in the solid state, with the thiadiazole ring pointing in the opposite direction of the O1-N3 coordination pocket [Fig. 1(top)]. The overall structure is practically planar, very likely triggered by the establishment of two intramolecular weak interactions, i.e. O1–H8···N3 and C7–H4···N1 (see Table S2, ESI), as indicated by the value of 10.68° for the C(7)-N(3)-C(6)-C(1) dihedral angle between the BTD and phenyl rings. Moreover, each two adjacent HL molecules in the crystal packing are coupled by weak intermolecular C–H···O type interactions (Figs. S1-S3, ESI). DFT calculations indicate that the global minimum equilibrium geometry corresponds indeed to the conformation observed in the solid state, noted as **A** hereafter, yet now the structure is fully planar (Fig. S4, ESI). Rotation of the thiadiazole unit around the N3–C6 bond generates a second stable **B** conformation, with the nitrogen atom N1 taking part to the coordination pocket along with O1 and N3, which is appropriate for chelation of a metal centre in a tridentate mode [Fig. 1 (bottom)]. This geometry, with a twist of 37.36° between BTD and the phenyl ring, very likely because of the repulsion between the imine H4 and benzene H3, is only 5.3 kcal mol^{-1}

higher in energy in the gas phase than the previous one, suggesting that the two conformations are in equilibrium in solution at room temperature (Table S3).

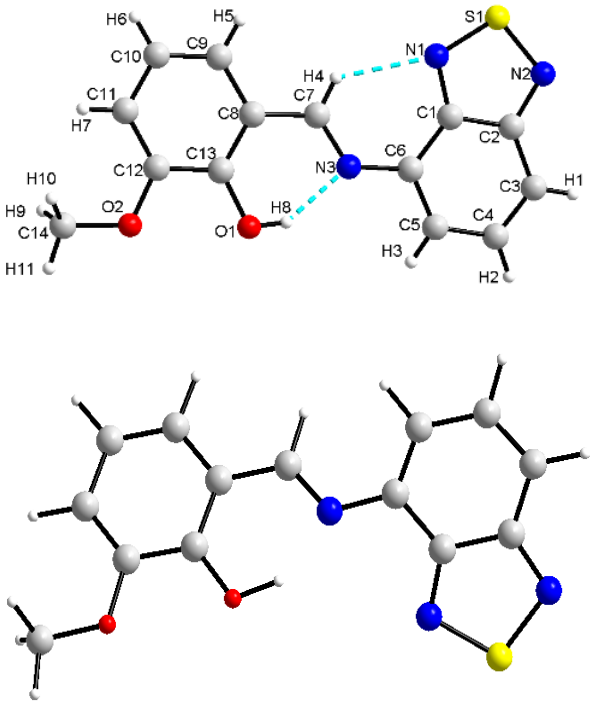

Fig. 1 Molecular structure of HL in the solid state (top) and its optimized conformation **B** (bottom).

Synthesis and characterization of the cobalt(II) complex

Considering that the phenolate form L is potentially a tridentate rigid ligand prone to afford octahedral neutral complexes of ML_2 type with certain divalent transition metals in a *mer* arrangement of the two ligands around the metal, we have considered the coordination of the deprotonated HL with cobalt(II). The cobalt (II) ion exhibits considerable coordination flexibility and a first-order spin-orbit coupling (SOC) or, in its absence, a sizeable zero-field splitting (zfs). These features are responsible for the extensive study of its complexes as candidates to mononuclear SMMs.[35,36,37,38,39,40,41,42]. Indeed, six-coordinate Co(II) mononuclear complexes showing octahedral (O_h), [43, 44, 45] trigonal prismatic (TP) [46, 47] or trigonal antiprismatic[48] coordination geometry are very good candidates for single-molecule magnets (SMMs). Usually, the octahedral complexes show a uniaxial anisotropy ($D < 0$) and only occasionally an easy-plane anisotropy ($D > 0$), but in all cases, the zfs is large.[49] Some of the latter cases behave as mononuclear SMMs.[35,36,39] In such cases, the zfs should govern the energy barrier (U_{eff}) that controls the slow magnetic relaxation. However, the experimental U_{eff} is significantly lower than $2D$, the energy barrier for a high-spin d^7 cobalt(II) complex. The case of ML_2 complexes based on rigid tridentate ligands, necessarily adopting a *mer* configuration,

is very interesting and they can show either negative[50] or positive zero-field splitting,[51] depending on the degree of distortion from O_h to D_3 symmetry.

The reaction of HL with cobalt(II) acetate in the presence of triethylamine provided the complex of formula $[CoL_2]\cdot CH_2Cl_2$ (**1**), which crystallizes in the triclinic *P*–1 space group, with a molecule of complex and one non-coordinated molecule of dichloromethane in the asymmetric unit (Fig. 2, Fig. S5a). The coordination environment of the cobalt centre is a distorted octahedron (Fig. S5b), the SHAPE analysis[52] indicating that it is closer to octahedral (S-O_h = 1.37) than to trigonal prismatic geometry (S-D_{3h} = 10.17). The Co–N and Co–O bond lengths vary between 2.088(4)–2.248(4) and 1.997(3)–2.004(3) Å, respectively (Table S4). The *cis*-angles cover the range 77.64(15)-105.46(14)°, whereas the *trans* ones go from 159.13(15) to 167.54(14)°. The bond-valence-sum (BVS) analysis,[53,54] with a value of 2.08 here, indicates a +2 oxidation state for the cobalt ion.

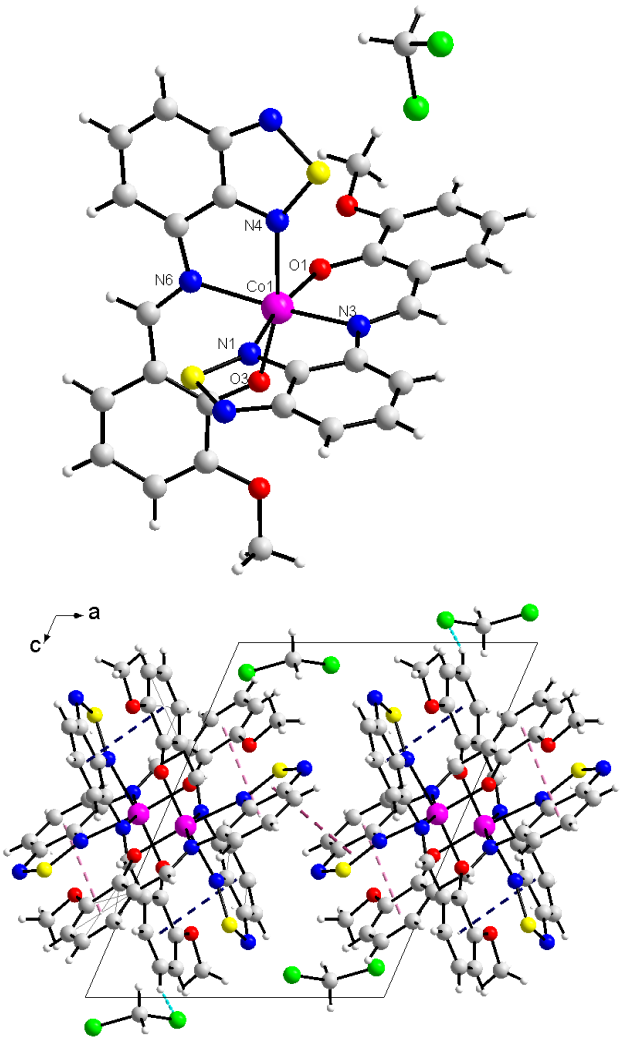

Fig. 2 (Top) Crystal structure of $[CoL_2]\cdot CH_2Cl_2$ (**1**). (Bottom) A view of the π···π phenolate-BTD rings (3.55 Å, pink), π···π phenolate-BTD rings (3.52 Å, blue), π···π TD-TD rings (3.67 Å, violet) and C–H···Cl type interactions (light blue) in the crystal packing.

Adjacent complexes are interconnected in the packing by π-π interactions between phenolate and BTD rings (3.55 and 3.52 Å) and by thiadiazol-thiadiazol π-π interactions (3.67 Å) (Fig. 2, Fig. S6-S7). Furthermore, the molecules of solvent establish weak C–H···Cl type interactions with one of the phenolate rings (Figs. 2 and S6-S7 and Table S5, ESI).

Static (dc) magnetic properties

As mentioned before, such neutral octahedral CoL_2 complexes, L being a tridentate ligand, are good candidates for single-molecule magnets (SMMs) whose magnetic study is carried out by static (dc) and dynamic (ac) magnetic measurements. The dc magnetic properties of **1** in the form of $\chi_M T$ against T plot [χ_M being the magnetic susceptibility per cobalt(II) ion] are shown in Fig. 3. At room temperature, the value of $\chi_M T$ is equal to 2.27 $cm^3\ mol^{-1}$ K. The fact that this value is larger than that calculated for a high-spin cobalt(II) ion (S_{Co} = 3/2) with g_{Co} = 2.0 using the spin-only formula [$\chi_M T = g_{Co}^2 S_{Co}(S_{Co}+1)$ = 1.874 $cm^3\ mol^{-1}$ K] is indicative of the existence of a significant orbital contribution to the magnetic moment.[55] Upon cooling down, $\chi_M T$ continuously decreases until it reaches a minimum value of 0.96 $cm^3\ mol^{-1}$ K at 1.9 K. No maximum of χ_M is observed over the whole temperature range explored. In the temperature range T > 20 K, the decrease of $\chi_M T$ on cooling is attributed to the depopulation of the higher-energy Kramers doublets arising from a spin-orbit coupling (SOC) in Co^{II} ions. Below 20 K, $\chi_M T$ takes values smaller than that of the expected limit (1.6 $cm^3\ mol^{-1}$ K) for this particular case, this feature pointing out the presence of antiferromagnetic interactions between Co^{II} ions. The occurrence in the crystal structure of **1** of π-π stacking interactions involving BTD, phenolate, and thiadiazol rings (values of the inter-ring distances in the range 3.52–3.67 Å) would provide a possible pathway for weak intermolecular magnetic interactions, the shortest cobalt-cobalt separation being 6.3207(13) Å. A supramolecular chain arrangement is developed along the crystallographic *b* axis in this case.

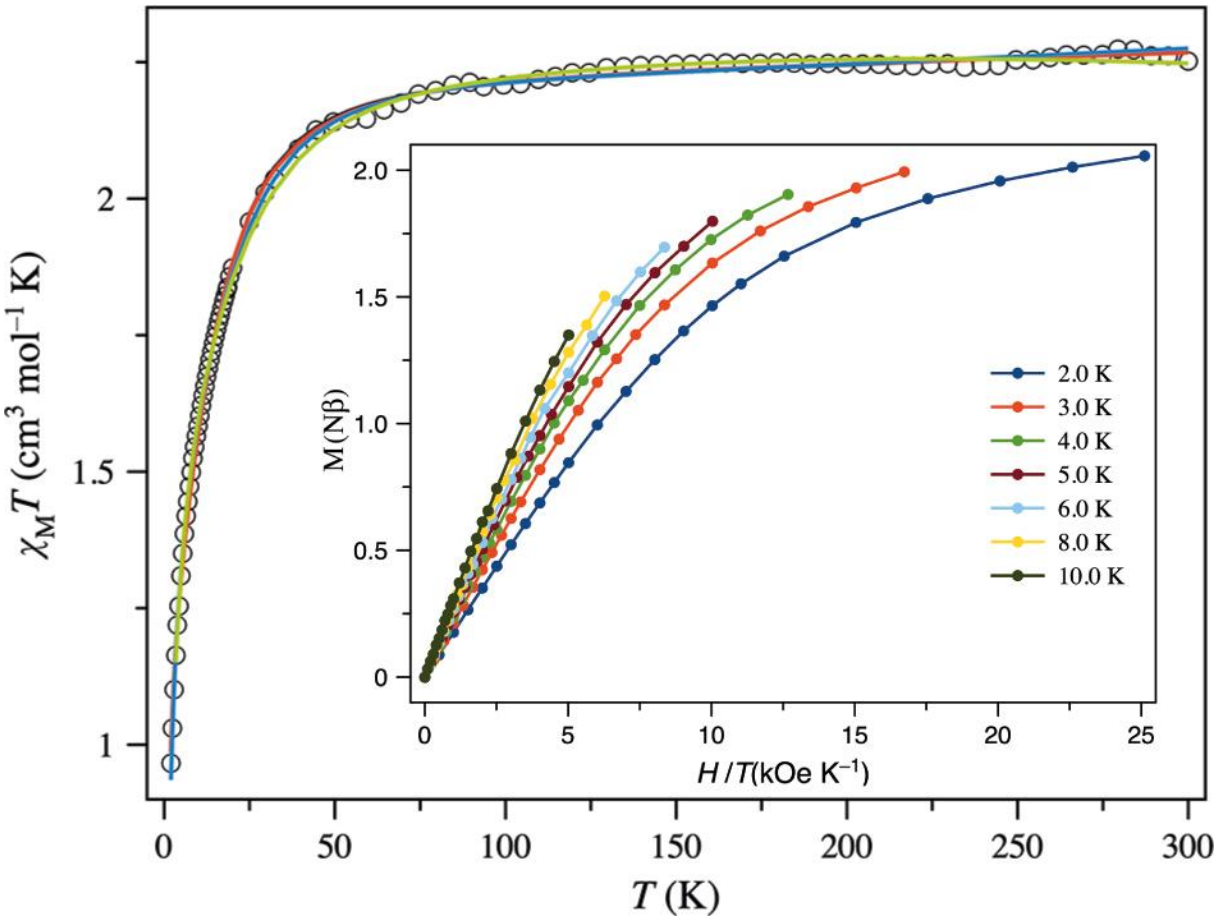

Fig. 3 Thermal dependence of the $\chi_M T$ product for **1**: (o) experimental data; (–) theoretical curve with the best fit through 1st-order SOC without (black) and with rhombicity (green) in the angular momentum, and zfs with $D > 0$ (red) and $D < 0$ (blue) models. Inset: Reduced magnetization in the temperature range 2.0-10.0 K. Solid lines are only eye-guides.

Having in mind that the magnetic behaviour of octahedral cobalt(II) complexes is generally induced by a first-order spin-orbit coupling (SOC), the use of the SOC Hamiltonian introduced through the T-P isomorphism is a suitable choice to analyse the magnetic properties of this cobalt(II) complex. This is why the magnetic susceptibility data of **1** were treated through the Hamiltonian of eq. (1)[56]

$$\boldsymbol{H} = -\alpha\lambda \boldsymbol{L}_{Co}\boldsymbol{S}_{Co} + \Delta[\boldsymbol{L}_{z,Co}^2 - L(L+1)/3] + \beta H(-\alpha \boldsymbol{L}_{Co} + g_e \boldsymbol{S}_{Co}) \qquad (1)$$

where λ is the spin-orbit coupling constant and α is an orbital reduction factor defined as $\alpha = A\kappa$. The κ parameter represents the reduction of the orbital momentum caused by the delocalization of the unpaired electrons, while A accounts for the mixing of the excited and ground $^4T_{1g}$ terms in the context of the splitting by the crystal field of the ^4F and ^4P terms of the free high-spin $3d^7$ cobalt(II) ion. It should be noted that A takes values between 1.5 and 1, which correspond to the limits of the weak and strong crystalline fields, respectively. Finally, Δ is the

energy difference between the singlet $^4A_2$ and doublet ^4E levels arising from the splitting of the ground $^4T_{1g}$ orbital triplet originated by an axial distortion of the ideal O_h coordination sphere. Second-order SOC splits these levels again, resulting into two and four Kramers doublets.

In the absence of an analytical law that connects the magnetic susceptibility with these SOC parameters, the former was simulated from numerical diagonalization of the energy matrix.[57] In such a situation, intermolecular magnetic interactions were included by adding a mean-field term (zj) to the $\chi_M T$ product. Best-fit parameters that simulate the experimental magnetic data of **1** in the whole temperature range explored [α = 1.136, Δ = 1165 cm^{-1}, λ = –124.6 cm^{-1} and zj = –0.17 cm^{-1} with F = 3.5 x 10^{-5} (F is the agreement factor defined as $\sum[(\chi_M T)_{exp} - (\chi_M T)_{calcd}]^2/\sum(\chi_M T)_{exp}]^2)$] provide a good agreement between theoretical and experimental curves (Fig. 3). Due to covalency effects, the λ value is smaller than that for the free ion (λ_0 = –180 cm^{-1}). Anyway, the values of all parameters are in the range of those reported for other six-coordinate high-spin cobalt(II) complexes.[56,58,59,60,61,62]

Alternatively, the experimental $\chi_M T$ *vs*. T data could also be analysed using a zero-field splitting (zfs) model characterized by axial (D) and rhombic (E) contributions. In octahedral cobalt(II) complexes, this model is usually applied below 120 K. Above that temperature, $\chi_M T$ can show a continuous and linear variation when cooling due to a depopulation of the most energetic levels arising from a more suitable 1st-order SOC model. In such cases, this last thermal dependence of $\chi_M T$ is phenomenologically described by a temperature-independent paramagnetism (TIP) term. Due to the difficulty of extracting a reliable value of E from the $\chi_M T$ *vs*. T data, the model was simplified as described by eq. (2):

$$\hat{H}_{zfs+Zeeman} = D\left[\hat{S}_z^2 - \frac{1}{3}S(S+1)\right] + E\left(\hat{S}_x^2 - \hat{S}_y^2\right) + \beta H\left[g_{\parallel}\hat{S}_z + g_{\perp}\left(\hat{S}_x + \hat{S}_y\right)\right] \qquad (2)$$

Once again, the theoretical $\chi_M T$ *vs*. T curve matches well the experimental one when intermolecular magnetic interactions (zj) are considered (Fig. 3). However, the sign of D cannot be determined from the thermal dependence of $\chi_M T$ when $g_{iso} = g_{\perp} = g_{\parallel}$ and so, the absolute value is provided (g_{iso} = 2.184, $|D|$ = 16.8 cm^{-1}, TIP = 123 x 10^{-6} cm^3 mol^{-1}, zj = –0.16 cm^{-1}, and F = 3.2 x 10^{-5}). But it is possible to determine this sign considering different values for $g_{\perp}$ and $g_{\parallel}$, and keeping $g_{\parallel}$ smaller for D > 0 and vice versa. Good agreements between theoretical and experimental curves are found for both signs of D, even if the concurrence is better for D < 0 attending to the agreement factor ($g_{\perp}$ = 2.223, $g_{\parallel}$ = 2.071, D = +18.5 cm^{-1}, TIP = 183 x 10^{-6} cm^3 mol^{-1}, zj = –0.17 cm^{-1}, and F = 3.2 x 10^{-5} *vs.* $g_{\perp}$ = 1.986, $g_{\parallel}$ = 2.433, D = –28.3 cm^{-1}, TIP = 336 x 10^{-6} cm^3 mol^{-1}, zj = –0.30 cm^{-1}, and F = 1.9 x 10^{-5}). Considering that each paramagnetic

site shows two neighbours in each supramolecular chain, that is $z = 2$, the magnetic interaction (j) would vary between –0.15 and –0.08 cm^{-1}. While the energy gap between the ground and the first excited Kramers doublets is 40.3 cm^{-1} for the 1st-order SOC model, it is ranged between 37.0 and 56.6 cm^{-1} in the *zfs* model, showing a good agreement between both models.

However, there is a discrepancy between the results from the two models. The concurrence using the SOC model is better for $\Delta > 0$ but for $D < 0$ in the zfs model.[35] However, in accordance with the geometry of the coordination sphere and the high value of the E/D ratio, there should be a substantial rhombicity. Introducing this rhombicity (ε) in the orbital momentum in the SOC model as if it were a zfs term,[35] the same as was done with the Δ parameter, the simulation with a negative value of Δ substantially improves ($\alpha = 1.284$, $\Delta = -3377$ cm^{-1}, $\varepsilon/\Delta = 0.108$, $\lambda = -111.6$ cm^{-1} and $zj = -0.38$ cm^{-1} with $F = 2.7 \times 10^{-5}$). In such a situation, the energy gap between the two first Kramers doublet is 50 cm^{-1}, close to the value found for $D < 0$. In conclusion, it is impossible to guarantee the sign of Δ, but the presence of a high rhombicity is established, which will be confirmed later by EPR spectroscopy (*vide infra*). In any case, a negative Δ value, also supported by the uniaxial zfs extrapolated from magnetometry and EPR spectroscopy, seems more reasonable.

The isothermal magnetization curves for **1** in the temperature range 2−10 K manifestly do not superimpose (inset Fig. 3), suggesting a moderate but not huge *zfs*. However, the intermolecular magnetic interactions, even if they are weak, also play a role on this feature. Moreover, the field dependence of the magnetization at 2.0 K reaches a near saturation value of Ms = 2.04 Nβ at 5 T. This value is smaller than the one expected for $S_{Co} = 3/2$ with $g = 2.0$ (that is 3.0 Nβ). The low-lying Kramers doublet, which is practically the only thermally populated below 20 K in cobalt(II) complexes in O_h symmetry, causes this discrepancy. Consequently, the magnetic susceptibility data below this temperature can be interpreted assuming an effective spin $S_{eff} = ½$ for this low-lying doublet.[63] According to eq. (3), the g-factor and the saturation magnetization for the effective doublet ground doublet with $\alpha = 1.184$ would be 4.12 and 2.06 Nβ respectively, values which are in agreement with the experimental data.

$$g = (10 + 2\alpha)/3 \qquad (3)$$

EPR spectroscopy

The Q-band EPR spectrum of **1** at 4.0 K is shown in Fig. 4. The weak EPR signals, which are hardly more intense than the white noise, match a uniaxial zfs ($D < 0$), agreeing with the

conclusions procured by the magnetometry. However, **1** should be EPR-silent for a null *E*/*D* ratio according to this situation. Thus, **1** should exhibit a certain rhombicity in the zfs tensor. The complexity of this spectrum and the weakness of the signals prevented any additional analysis. Even so, this spectrum was compared with that simulated for the ground Kramers doublet through an effective spin approach and using the values of the *g* components found by CASSCF/NEVPT2 calculations for a negative *D* (see below). Again, there is a qualitative agreement that supports a uniaxial zfs.

Regardless of a slight or moderate displacement of the theoretical signals from the experimental ones, the splitting of the experimental signals is the most remarkable fact. Possible causes include the presence of complexes with distinct electronic and magnetic features coming from different geometries or the concurrence of the low-lying excited states. Nevertheless, the X-ray structure of **1** shows a unique independent cobalt site, the needed geometrical changes should be big, and the *D* value is too large to consider an excited Kramer doublet close enough to exhibit a significant population. Thus, these alternatives can be ruled out. Previously, magnetometry evidenced the presence of weak intermolecular magnetic interactions, which will later be supported by a theoretical study (see below). Since both centres were assumed collinear, only an anisotropic spin-spin coupling may split the signals in the Q-band EPR spectrum.[64] The spin Hamiltonian that considers this coupling is summarized by eq. (4)

$$\hat{H}_S = \mu_B \vec{B} \boldsymbol{g}^{\boldsymbol{eff}} \left(\hat{S}_1^{eff} + \hat{S}_2^{eff}\right) + \hat{S}_1^{eff} \mathbf{D} \hat{S}_2^{eff} \qquad (4)$$

being **D** a traceless interaction tensor collinear to $\boldsymbol{g}^{\boldsymbol{eff}}$ and positive for antiferromagnetic coupling. The spectrum was successfully simulated with g_y = 2.55 and g_z = 6.50, values corresponding to an effective spin doublet and an anisotropic electron-electron spin-spin coupling between two of these effective spins **D** = [0.24, 0.50, 0.035] cm^{-1}. For two spins *S* = 3/2, these interactions must be approximately one-ninth of those found in this EPR study, being within the order of magnitude found by magnetometry.

However, from the Q-band EPR spectrum, we can only conclude that the value of the g_x component must be less than 1.0, essentially lower than the other two ones and in agreement with a uniaxial zfs ($D < 0$). However, the X-band EPR spectrum of the compound can provide better information about g_x (Fig. 4). Firstly, this spectrum roughly shows the same splitting of the signals associated with g_y and g_z from the Q-band EPR spectrum, leaving no doubt about the presence of an intermolecular electron-electron coupling.[64] Additionally, a split signal in the region from 10 to 13 kG is associated with a tiny g_x value of 0.55, in agreement with the previous conclusions. In summary, the EPR study allows us to establish a negative sign of *D*, a

high rhombicity or *E*/*D* ratio, and the presence of intermolecular magnetic interactions between close neighbours.

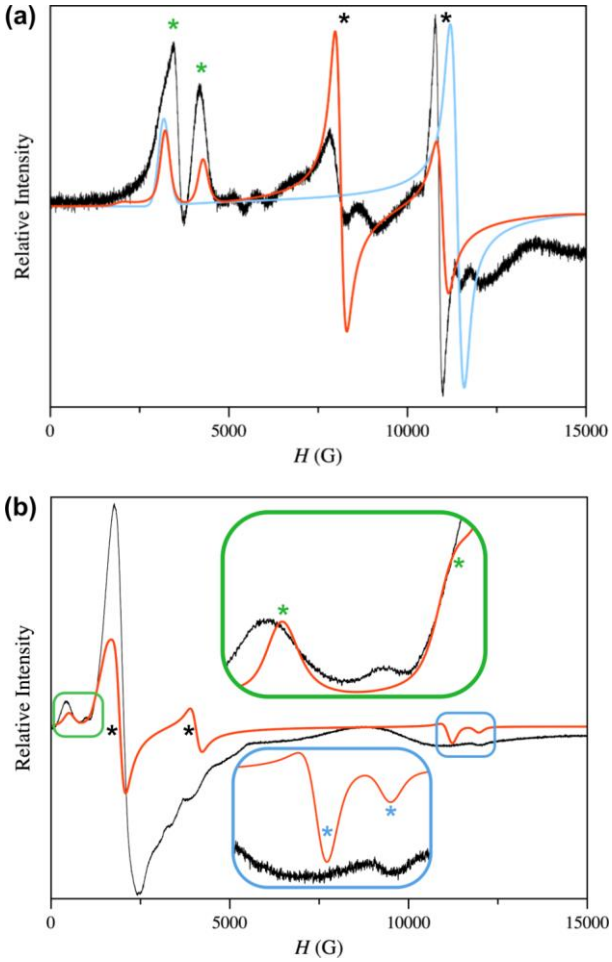

Fig. 4 Q (a) and X-band (b) EPR spectra (black lines) of a powdered sample of **1** at 4.0 K. The blue line (a) represents the simulation with the parameters for the ground Kramer doublet procured from CASSCF/NEVPT2 calculations (g_x = 1.49, g_y = 2.14, and g_z = 7.67). According to eq. (4), the red lines correspond to the best simulations with the parameters $\boldsymbol{g}^{eff}$ = [0.55, 2.55, 6.50] and **D** = [0.24, 0.50, 0.035] cm^{-1}. Signals marked with green, black and blue asterisks coincide with g_x, g_y, and g_z, respectively. Rounded square boxes show enlargements of certain field regions.

Theoretical calculations

DFT calculations on dimeric entities built from the experimental crystal structure ($d_{Co\cdots Co}$ = 6.457 Å) were conducted in order to validate the existence of antiferromagnetic intermolecular magnetic interactions through π-π stacking of the BTD ligand developing a one-dimensional behaviour along the crystallographic *b* axis. Cg1-Cg2 and Cg3-Cg4 contacts are responsible for the intermolecular magnetic coupling (Fig. S7). The analysis of these intermolecular contacts is summarized in Table S6. The fact that the two quasi-planar BTD ligands (maximum deviation of the mean plane: 0.30 Å) from neighbouring complexes are

almost parallel (α ca.8º) and their closeness (Cg-plane shorter than 3.4 Å) make possible a weak magnetic coupling. Thus, the value for the magnetic coupling constant calculated from the B3LYP functional is j = –0.07 cm^{-1}. Similar values are found using its long-range corrected version (CAMB3LYP, j = –0.04 cm^{-1}) or that in the geometry optimization PBE1PBE hybrid functional (j = –0.08 cm^{-1}). They all agree well with that found from experimental data (from –0.15 to –0.08 cm^{-1}). Opposite spin densities of the atoms involved in the shortest contacts are usually found through intermolecular π- π stacking. A visualization of the stacking between adjacent complexes shows short contacts between atoms from BTD ligands with spin densities with the same sign in the mononuclear fragment (Fig. 5). Therefore, the natural reversal spin alignment leads to an antiferromagnetic interaction, as previously concluded.

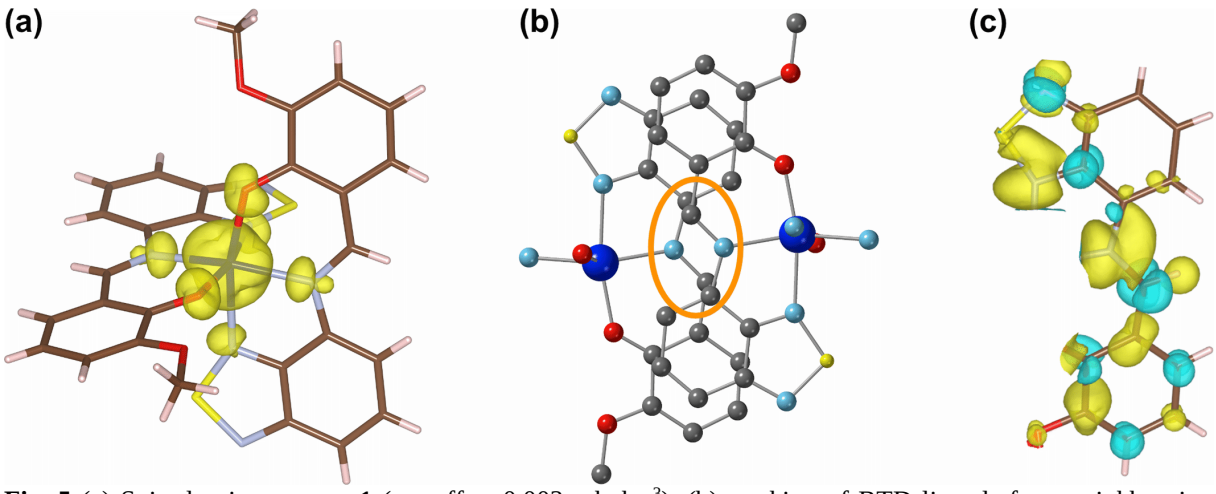

Fig. 5 (a) Spin density map on **1** (cut-off at 0.003 e bohr^{-3}), (b) stacking of BTD ligands from neighbouring complexes, and (c) zoom centred on the BTD ligand of the spin density map (cut-off at 0.0002 e bohr^{-3}). Orange oval in (b) indicates the region with the largest atomic spin densities and some of the shortest contacts. Positive and negative spin densities in (a) and (c) are displayed in yellow and blue colours. Hydrogen atoms are omitted in (b) for clarity.

Theoretical CASSCCF/NEVPT2 calculations were performed to confirm the sign and magnitude of the D parameter as well as the E/D quotients of **1**. These calculations provide a large and negative value for D (–57.3 cm^{-1}), but since the value of E/D ratio (0.300) is close to its maximum value (1/3), the sign of D is meaningless. According to the negative value of D, this large *zfs* is translated into the calculated g-tensor, being the perpendicular component substantially smaller than the parallel one ($g_{\perp}$ = 2.172 and $g_{\parallel}$ = 2.804). The electronic configuration for the high-spin ground state of **1**, from which quadruplet excited states are generated by promoting an electron from a fully occupied orbital to a half-occupied one, is shown in Fig. S8 (ESI). The M_s wavefunctions of these and other doublet excited states can mix

with those from the ground state through a SOC Hamiltonian, leading to a zfs in the latter. The more significant spin-orbit contributions mainly originate from the quartet states (D_Q) – more specifically from the two first excited states (Q_1 and Q_2), rather than from the doublet ones (D_D), the relative energy of each excited state (Δ_i) governing the magnitude of its input (Table S7). Due to some geometrical distortions, the $^4T_{1g}$ ground state splits into the ground, and the Q_1 and Q_2 excited states. Then, these excited states are very close to the ground one (746 and 1971 cm^{-1}), and their contributions to *D* are significantly larger. Contributions of other excited states are almost negligible because they are far above the ground state on the energy scale. On the other hand, the great energy gap arising between two components in the ^4E level leading to place Q_1 almost equidistant from the ground and Q_2 states is the cause of a more significant *zfs* rhombicity in **1** (Table S7). The large *E*/*D* ratio is related to the important geometrical distortions in the coordination sphere, as shown by the *cis*- and *trans*- angles (*ca*. 77-105º and 159-168º) that deviate significantly from the ideal ones (90 and 180 º), and the presence of several types of competing donor atoms with different ligand-field strength competing. All these factors cause the orientation of the *zfs* tensor that does not coincide with any of the metal-ligand bond directions (Fig. S9). As a last remark, the calculations lead to an average g_{eff} value for the ground Kramers doublet (3.77) which is larger than that for the excited one (3.39) and closer to that estimated through magnetometry (4.12). Although in qualitative agreement with the experimental results, these values significantly deviate from them. Finally, it is worth noting that the values of the *g*-factor components calculated for the ground Kramers doublet (S_{eff} = ½) simulate quite well the signals recorded from the experimental EPR spectrum (Fig. 4), a feature that validates the negative sign of *D*.

Partial charge transfers in the ground and closest excited states or a deficient description of the *d* orbitals can lead to remarkable changes in the zfs for some cases. In such examples, it is necessary to expand the active space to consider the new contributions to the zfs from this electronic feature. In this way, one empty or one filled molecular orbital is added to reach the space actives with five or seven electrons, respectively, in six orbitals [(5,6) or (7,6)]. Specifically, forty of the early LUMOs and also HOMOs, including also those more diffuse *d* orbitals that constitute a double *d* shell, were tested for expanding the active space.[65] However, this methodology, which allowed improving the estimation of *D* in a high-spin d^5 iron(III) complex with large zfs,[66] does not report any advance here. Thus, values of *D* in these new 80 calculations, ranging from –57.9 to –56.2 cm^{-1}, were similar to that found from the original active space, the changes being not significant. Nevertheless, the magnitude of *D* matches better when the zfs is calculated on the optimized geometry but not its sign (D = +34.9 cm^{-1}, $g_\perp$ =

2.423, $g_{\|}$ = 2.105, and g_{eff} = 3.935). Finding an explanation for this improvement is not evident. A possible cause could be that the optimized molecular geometry of the complex were more similar to that occurring at low temperatures. Nevertheless, it is known that there are some discrepancies (mainly longer metal-ligand bonds) between DFT optimized and real geometries, which can cause certain inaccuracies in the electronic structure corrected by geometry optimization.

Dynamic (ac) magnetic properties

In order to explore the possible occurrence of slow magnetic relaxation in $[CoL_2]\cdot CH_2Cl_2$, alternating current (ac) magnetic susceptibility measurements were carried out as a function of the frequency (ν) of the oscillating magnetic field (±5.0 G) in the temperature range 2.0–7.0 K under applied H_{dc} fields of 0, 1000, and 2500 G. These measurements in the absence of a magnetic field, H_{dc} = 0 G, show the lack of out-of-phase signals (χ_M”), suggesting the presence of quantum tunnelling magnetization effects (QTM). Applying dc magnetic fields of 1000 and 2500 G cancels this effect and causes the appearance of frequency-dependent χ_M” signals as shown in Figs. 6 and S10 (ESI) for H_{dc} = 1000 and 2500 G, respectively.

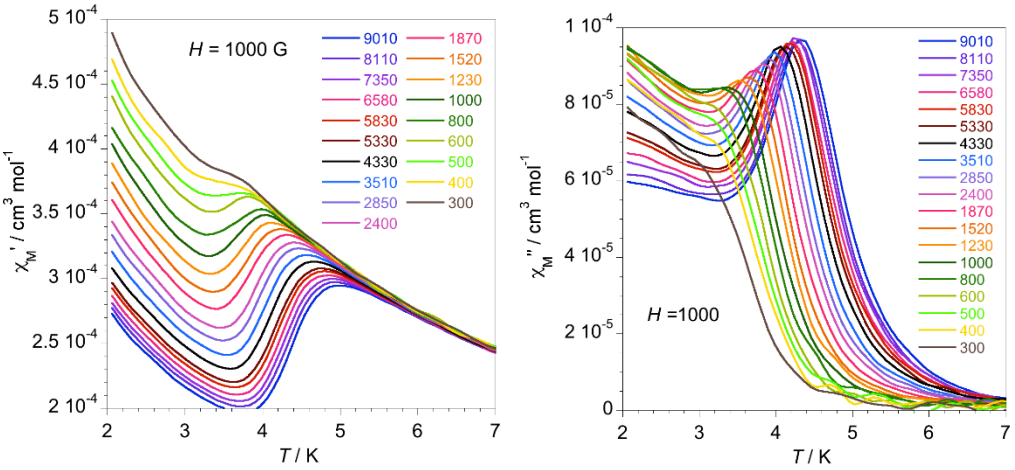

Fig. 6 Frequency dependence of the in-phase (left) and out-of-phase (right) components of the magnetic susceptibility of **1** under a static magnetic field H_{dc} = 1000 G with an oscillating field ±0.5 G and at the indicated frequencies.

These plots show maxima of χ_M” that depend on T and frequency (ν), which is the typical behaviour of a SIM/SMM. Indeed, a relaxation process (HT) is observed above 3.0 K, and then, at lower temperatures, a new increase of χ_M” occurs, denoting the arrival of a second competing relaxation process (LT). Since the frequency indirectly corresponds to the relaxation time ($\tau^{-1} = 2\pi\nu_{max}$) and the temperature for the χ_M” maximum, the spin reversal blockage, a τ *vs.* T table

can be established. However, the lack of maxima for the LT process prevents its analysis. According to a relaxation governed by an Orbach mechanism, these data should follow an Arrhenius law as expressed by eq. (5)

$$\tau^{-1} = \tau_0^{-1} \exp(-E_a/kT) \qquad (5)$$

where τ_0 is the pre-exponential coefficient or the relaxation time when E_a/kT is null, E_a is the energy barrier controlling the spin reversal. At high temperatures, plots of ln(τ) as a function of $1/T$ (Fig. S11) obey this law with values of 2.0 x 10^{-9} s and 27.7 cm^{-1} (1000 G) and 9.4 x 10^{-10} s and 29.5 cm^{-1} (2500 G). Both τ_0 and E_a values are of the same order of magnitude as those obtained in previous works with other mononuclear six-coordinate high-spin cobalt(II) compounds.[45] However, this energy barrier is significantly lower than expected from the zfs ($2D$ = 56.6 cm^{-1}). A deviation from the Arrhenius law at low temperatures, not visualized here, has its origin in the possible intervention of other relaxation processes that will be subject of further analysis.

There is another more appropriate way to study the dynamic magnetic behaviour. It entails using the generalized Debye model to analyze in unison the isothermal frequency dependences on in- (χ_M') and out-phase (χ_M") components of the *ac* susceptibility, that is, the χ_M' and χ_M" *vs.* ν curves, and also the dependence between them through the Argand plots. These plots are shown in Fig. S12. Below 4.0 K, an asymmetry arises in the Argand plots, mainly under magnetic fields of 1.0 and 2.5 kOe, suggesting two-step relaxation processes, one of them becoming only apparent at lower temperatures in agreement with the conclusions reached from the thermal dependence on these ac susceptibility components. Thus, magnetic data were simulated considering two relaxation contributions to the generalized Debye model. Nevertheless, it was impossible to distinguish the LT relaxation process under a dc magnetic field of 5.0 kOe.

The Arrhenius plots for the LT relaxation show a linear dependence for a thermally-assisted Orbach mechanism (Fig. S13). The best-fits (Table S8) provide long relaxation times (10^{-4} s) and too low energy barriers ($\approx$ 2 cm^{-1}). However, one should be careful with these values because of the difficulty of extracting them from experimental data and their relatively large standard deviations. However, the HT relaxation exhibits two patterns corresponding to two different and competing mechanisms (Fig. S13). One of them unveils a linear thermal dependence with a higher energy barrier ($E_a \approx 35$ cm^{-1}) and shorter relaxation times ($\tau_0 \approx 10^{-10}$ s) than those found for the LT relaxation but in agreement with those obtained from the former analysis. The other one, slower ($\tau_0 \approx 10^{-4}$ s) and temperature independent, occurs below 3.0 K

and it corresponds to a quantum tunnelling (QT, $\tau^{-1} = \tau_{0,QT}^{-1}$) that avoids the energy barrier set by the zfs. Under a dc magnetic field of 5.0 kOe, both relaxation steps fuse combining two Orbach mechanisms [$\tau^{-1} = \tau_{0,1}^{-1} \exp(-E_{a,1}/kT) + \tau_{0,2}^{-1} \exp(-E_{a,2}/kT)$] and hiding the QT relaxation, which may have disappeared due to the effect of the high applied magnetic field. In such a case, the values of E_a and τ_0 are similar to those found for the LT and HT relaxation under lower magnetic fields (Table S8).

Despite the linear correlations found in the Arrhenius plots suggesting Orbach mechanisms play a role in the magnetic relaxation, both HT and LT energy barriers are essentially lower than expected from zfs, mainly in the former one. Although one might think that relaxation can occur through vibrational modes with energies close to the energy barriers, the value of $E_{a,2}$ or $E_{a,LT}$ is even too low (≈ 2 cm^{-1}, Table S8). This characteristics makes it necessary to test other alternatives such as direct ($\tau^{-1} = A \cdot T$) or Raman-type ($\tau^{-1} = C \cdot T^n$) relaxation mechanisms. The best way to do it is to use ln(τ) vs. ln(T) plots (Fig. 7 and S13), which should exhibit linear dependence with slopes equal to 8 or 9 and 2 (n) for Raman relaxations assisted by acoustic and optical phonons, or one and null for direct and quantum-tunnelling processes. Occasionally, several mechanisms can act in the same temperature region, fading the assumed linear dependences. However, this is not the case for **1**. Whereas the HT relaxation under lower dc magnetic fields is governed by a combination of Raman and quantum-tunnelling processes, the LT relaxation for any working *dc* magnetic field fits well with a single Raman mechanism with n_2 values from 1.0 to 1.9 (Table S9). Instead, n_1 takes values close to eleven in the HT relaxation. The n_2 value of 1.9 at 1.0 kOe for the LT relaxation points to a Raman mechanism assisted by optical phonons. However, the rest of the n_2 values are closer to unity, and the uncertainty associated with the complex analysis makes us think instead of a direct mechanism. Thus, the QT process is not registered under a *dc* magnetic field of 5.0 kOe, HT and LT relaxations fuse, and an unambiguous direct mechanism emerges. Similarly, the n_1 value for the HT relaxation is slightly oversized, but, at 5.0 kOe, it is reduced to that expected for a Raman mechanism assisted by phonon acoustic (Table S9). In short, the magnetic relaxation in **1** is governed by competing quantum-tunnelling, direct and Raman processes, the latter being operative above 4.0 K.

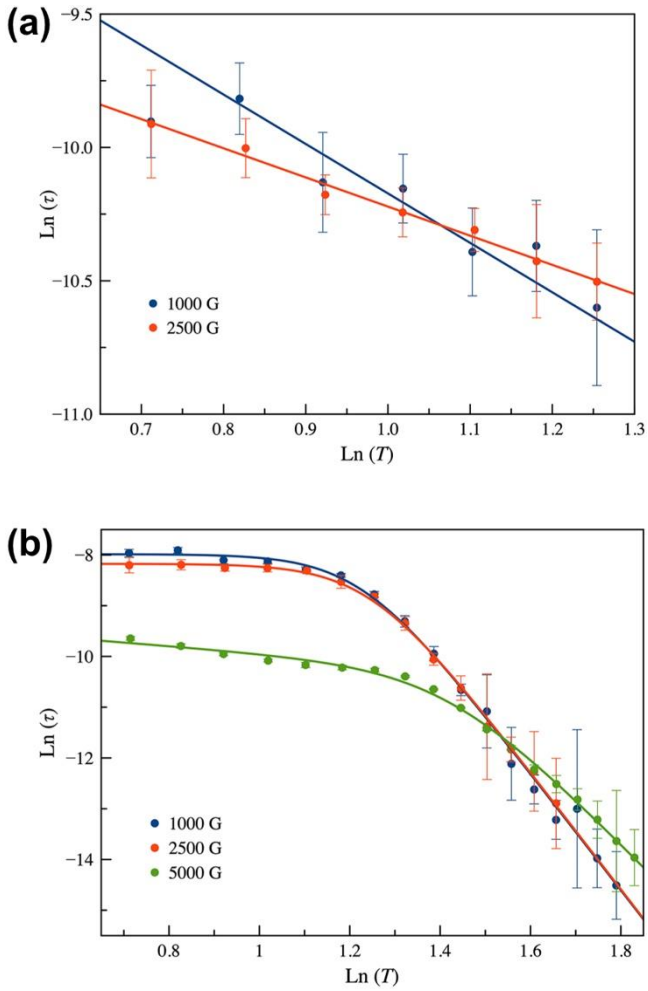

Fig. 7 Ln(τ) *vs* ln(T) plots for the calculated magnetic relaxation times (τ) of **1** under *dc* static fields of 1.0 (blue), 2.5 kOe (red), and 5.0 kOe (green) for the two competing relaxation processes, one of them predominating at low temperatures (a) and other at higher ones (b). Standard deviations appear as vertical error bars. Solid lines are the best-fit curves simulated by combinations of quantum-tunnelling and Raman mechanisms. More details in the main text.

Conclusions

The unprecedented π-conjugated benzothiadiazole Schiff base ligand HL, prepared by a straightforward strategy involving the reaction of 4-amino-benzothiadiazole with *ortho*-vanillin, is provided with interesting abilities as tridentate monoanionic *NNO* ligand in its phenolate form. We have investigated in this work its neutral cobalt(II) complex CoL_2 where the metal ion is bis(chelated) by two ligands within a slightly distorted octahedral coordination geometry. The importance of the π-conjugated heterocyclic framework is highlighted in the solid state by the establishment of π-π interactions between the phenolate and BTD units and between the thiadiazole rings. The π-π stacking of the BTD ligands promotes the existence of antiferromagnetic intermolecular magnetic interactions, with a DFT calculated value for the

magnetic coupling j = –0.07 cm^{-1}, in agreement with that found from the experimental data. The static magnetic behaviour of the complex can be analysed either by considering a spin-orbit coupling mechanism or a zero-field splitting one. Ac magnetic susceptibility measurements show the presence of out-of-phase signals upon applying dc magnetic fields of 1000 and 2500 G, thus indicating that the mononuclear complex CoL_2 constitutes a new example of field-induced mononuclear single-molecule magnet (SMM). Further work will be devoted to the investigation of other metal centres and the attachment of two *ortho*-vanillin fragments on the BTD platform.

Experimental

General procedures

All the reactions were carried out under ambient conditions with HPLC-grade solvents. Nuclear magnetic resonance spectra were recorded on a Bruker Avance DRX 300 spectrometer operating at 300 and 75 MHz for ^1H and ^{13}C, respectively. Chemical shifts are expressed in parts per million (ppm) downfield from external TMS. The following abbreviations (δ) are used: s, singlet; d, doublet; t, triplet; m, massif. MALDI-TOF MS spectra were done on a Bruker Biflex-IIITM apparatus, equipped with a 337 nm N_2 laser. Elemental analysis were recorded using a Flash 2000 Fisher Scientific Thermo Electron analyzer. The IR spectra were performed on an ATR Bruker Vertex 70 spectrophotometer in the range 4000-400 cm^{-1}. Signal intensities (height) are denoted by the following abbreviations: vs-very strong, s-strong, m-medium and w-weak.

Synthesis

2-[(2,1,3-benzothiadiazol-4-ylimino)methyl]-6-methoxyphenol (HL). 4-amino-2,1,3-benzothiadiazole **3** (4.97 g, 32.86 mmol) was dissolved in ethanol, and then *ortho*-vanillin (4.97 g, 32.86 mmol) was added. The mixture was stirred at 80 °C during 4 h. The orange-red precipitate formed during the reaction was filtered off and washed with ethanol. Yield: (7.59 g, 81%). Elemental Analysis calcd. (%) for $C_{14}H_{11}N_3OS$: C, 58.93; H, 3.89; S, 11.24; N, 14.73. Found: C, 58.72; H, 3.93; S, 11.29; N, 14.96. IR (ATR, cm^{-1}): 2933w, 1592s, 1570s, 1516s, 1463m, 1448vs, 1418vs, 1338m, 1320m, 1271vs, 1252s, 1211vs, 1169m, 1154m, 1066s, 1047s, 964s, 904s, 834vs, 808vs, 781vs, 741vs, 728vs, 652m, 622m, 600m, 557m, 511s, 492vs. Exact mass, m/z 285.0571. ^1H NMR (300 MHz, $CDCl_3$) δ: 13.85 (s, 1H), 9.59 (s, 1H), 7.92 (d, J = 8.8 Hz, 1H), 7.70 – 7.63 (m, 1H), 7.49 (d, J = 8.0 Hz, 1H), 7.14 (d, J = 7.7 Hz, 1H), 7.04 (d, J

= 8.0 Hz, 1H), 6.93 (t, J = 7.9 Hz, 1H), 3.97 (s, 3H). ^{13}C NMR (76 MHz, $CDCl_3$) δ: 166.94, 156.41, 152.00, 149.81, 148.71, 139.18, 129.98, 124.53, 122.20, 119.97, 119.53, 118.83, 115.47, 56.42.

[CoL_2] complex (1). To a red-orange solution of HL (20 mg, 0.070 mmol) and triethylamine (0.01 mL, 0.070 mmol) in methylene chloride (3 mL), was added a solution of cobalt(II) acetate tetrahydrate (9 mg, 0.035 mmol) in methanol (3 mL). The reaction mixture was magnetically stirred at 65 °C for 2 hours. After 1-3 days of slow evaporation, brown needle-shaped crystals of the complex [CoL_2]·CH_2Cl_2 were collected by filtration. Yield: 15 mg (61.0 %). Elemental Analysis calcd. (%) for $C_{29}H_{22}Cl_2CoN_6O_4S_2$: C, 48.89; H, 3.11; S, 9.00; N, 11.80. Found (%): C, 49.12; H, 2.98; S, 9.12; N, 12.65. IR (ATR, ν_{max} cm^{-1}): 1740m, 1585s, 1526s, 1419vs, 1395vs, 1236s, 1201vs, 1166s, 1079s, 1059s, 977m, 900m, 846s, 800m, 732vs, 666m, 597m, 547m, 522m, 512m, 486m, 413m. MALDI-TOF MS: m/z = 343.0 [CoL]$^+$.

DFT study on HL and [CoL_2]·CH_2Cl_2: Geometries and magnetic interactions

Optimized geometries for the HL ligand and the [CoL_2] complex were performed using the Gaussian 09 package,[67] with the PBE1PBE functional[68] and TZVP[69,70] basis set. These optimized geometries were then confirmed as global minima by frequency calculations. Starting geometries for both ligand and complex were derived from the X-ray structure. For the calculations on the [CoL_2] complex, a polarizable continuum model (PCM) was used with the parameters corresponding to the acetonitrile in order to avoid the usual electronic overdelocalization in DFT calculations.[71]

Intermolecular magnetic interactions through π-π stacking of the BTD ligand of two neighbouring mononuclear complexes were performed on the crystallographic coordinates. This study was also carried out by DFT type calculations through the Gaussian 09 package by using the PBE1PBE, also hybrid B3LYP, and its long-correlated version CAM-B3LYP functionals,[68,72,73,74,75] the quadratic convergence approach and a guess function generated with the fragment tool of the same program.[67] The magnetic coupling states were obtained from the relative energies of the broken-symmetry (BS) singlet spin states from the high-spin state with parallel local spin moments (6j). More details about the broken-symmetry approach to evaluate the magnetic coupling constants can be found in the literature.[76,77,78]

Ab initio calculations on the *zfs* tensor in [CoL_2]·CH_2Cl_2

The parameters that determine the axial (D) and rhombic (E) components of the local zero-field splitting (*zfs*) of **1** were estimated from theoretical calculations based on a second-

order *N*-electron valence state perturbation theory (CASSCF/NEVPT2),[79,80,81] which often provides accurate values of the nearby excited states energies and for the *zfs* tensor of mononuclear first-row transition metal complexes. Calculations were carried out on the experimental geometries with version 4.0.1 of the ORCA programme[82] using the def2-TZVP basis set proposed by Ahlrichs[70,83] and the auxiliary TZV/C Coulomb fitting basis sets.[84,85,86] The contributions to *zfs* from 10 quartet and 20 doublet excited states generated from an active space with seven electrons in five *d* orbitals were included using an effective Hamiltonian. RIJCOSX method was used combining resolution of the identity (RI) and ”chain of spheres” COSX approximations for the Coulomb and exchange terms, respectively.[87,88,89]

Magnetic measurements and EPR spectroscopy

Variable-temperature (300-1.9 K) direct current (dc) magnetic susceptibility measurements under applied fields of 0.1 (T < 0 K) and 1.0 kG ($T \geq 50$ K) and variable-field (0-5 T) magnetization measurements at 2.0 K for a polycrystalline sample of $[Co(L)_2]\cdot CH_2Cl_2$ where carried out with a Quantum Design SQUID magnetometer. Alternating current (ac) magnetic susceptibility measurements under different applied dc magnetic fields covering the 0-2500 G at low temperatures (2.0-7.0 K) were performed with a Quantum Design Physical Property Measurement System (PPMS). The magnetic susceptibility data were corrected for the diamagnetism of the constituent atoms and the sample holder (a plastic bag). Dc and ac measurements were done by crushing the crystals in order to prevent any displacement caused by the magnetic anisotropy. The Q- and X-band EPR spectra of a powdered sample of $[Co(L)_2]\cdot CH_2Cl_2$ was registered at 4.0 K with a Bruker ER 200 spectrometer equipped with a helium continuous-flow cryostat. Spectra were simulated using the Matlab toolbox EasySpin.[90]

ORCID

Nataliya Plyuta: 0000-0002-1835-5956
Svitlana Petrusenko: 0000-0001-8594-2643
Vladimir Kokozay: 0000-0003-1834-3020
Thomas Cauchy: 0000-0003-4259-3257
Francesc Lloret: 0000-0003-2959-0879
Miguel Julve: 0000-0001-9006-8268
Joan Cano: 0000-0002-7382-7135
Narcis Avarvari: 0000-0001-9970-4494

Conflicts of interest

There are no conflicts of interest to declare.

Acknowledgements

This work was supported in France by the CNRS, the University of Angers, in Ukraine by the Ministry of Education and Science, the Taras Shevchenko National University of Kyiv and the French Embassy in Kyiv (grant to N.P.). Financial support in Spain from the Ministerio Español de Ciencia, Innovación y Universidades (Project PID2019-109735GB-I00 and Unidad de Excelencia María de Maetzu CEX2019-000919) and the Generalitat Valenciana (Project AICO/2020/183) is gratefully acknowledged.

Notes and references

1 C. T. Chen, *Chem. Mater.*, 2004, **16**, 4389–4400.

2 B. A. D. Neto, A. A. M. Lapis, E. N. da Silva Júnior and J. Dupont, *Eur. J. Org. Chem.*, 2013, 228–255.

3 M. Velusamy, K. R. J. Thomas, J. T. Lin, Y. Hsu and K. Ho, *Org. Lett.*, 2005, **7**, 1899–1902.

4 L.-Y. Lin, Y.-H. Chen, Z.-Y. Huang, H.-W. Lin, S.-H. Chou, F. Lin, C.-W. Chen, Y.-H. Liu and K.-T. Wong, *J. Am. Chem. Soc.*, 2011, **133**, 15822–15825.

5 S. Haid, M. Marszalek, A. Mishra, M. Wielopolski, J. Teuscher, J.-E. Moser, R. Humphry-Baker, S. M. Zakeeruddin, M. Grätzel and P. Bäuerle, *Adv. Funct. Mater.*, 2012, **22**, 1291–1302.

6 Y. Geng, F. Pop, C. Yi, N. Avarvari, M. Grätzel, S. Decurtins and S.-X. Liu, *New J. Chem.*, 2014, **38**, 3269–3274.

7 T. Kono, D. Kumaki, J. Nishida, T. Sakanoue, M. Kakita, H. Tada, S. Tokito and Y. Yamashita, *Chem. Mater.*, 2007, **19**, 1218–1220.

8 M. Zhang, H. N. Tsao, W. Pisula, C. Yang, A. K. Mishra and K. Müllen, *J. Am. Chem. Soc.*, 2007, **129**, 3472–3473.

9 Y. Geng, R. Pfattner, A. Campos, J. Hauser, V. Laukhin, J. Puigdollers, J. Veciana, M. Mas-Torrent, C. Rovira, S. Decurtins and S.-X. Liu, *Chem. Eur. J.*, 2014, **20**, 7136–7143.

10 K. R. J. Thomas, J. T. Lin, M. Velusamy, Y.-T. Tao and C.-H. Chuen, *Adv. Funct. Mater.*, 2004, **14**, 83–90.

11 B. A. D. Neto, P. H. P. R. Carvalho and J. R. Correa, *Acc. Chem. Res*., 2015, **48**, 1560–1569.

12 D. Aldakov, M. A. Palacios and P. Anzenbacher, Jr., *Chem. Mater.*, 2005, **17**, 5238–5241.

13 S. Uchiyama, K. Kimura, C. Gota, K. Okabe, K. Kawamoto, N. Inada, T. Yoshihara and S. Tobita, *Chem. Eur. J.*, 2012, **18**, 9552–9563.

14 F. Pop, A. Amacher, N. Avarvari, J. Ding, L. M. Lawson Daku, A. Hauser, M. Koch, J. Hauser, S.-X. Liu and S. Decurtins, *Chem. Eur. J.*, 2013, **19**, 2504–2514.

15 F. Pop, S. Seifert, J. Hankache, J. Ding, A. Hauser and N. Avarvari, *Org. Biomol. Chem.*, 2015, **13**, 1040–1047.

16 M. R. Ams, N. Trapp, A. Schwab, J. V. Milić and F. Diederich, *Chem. Eur. J.*, 2019, **25**, 323–333.

17 N. W. Alcock, A. F. Hill and M. S. Roe, *J. Chem. Soc. Dalton Trans*., 1990, **5**, 1737–1740.

18 M. W. Renner, K. M. Barkigia, D. Melamed, K. M. Smith and J. Fajer, *Inorg. Chem.*, 1996, **35**, 5120–5121.

19 M. Munakata, T. Kuroda-Sowa, M. Maekawa, M. Nakamura, S. Akiyama and S. Kitagawa, *Inorg. Chem*., 1994, **33**, 1284–1291.

20 G. S. Papaefstathiou, A. Tsohos, C. P. Raptopoulou, A. Terzis, V. Psycharis, D. Gatteschi and S. P. Perlepes, *Cryst. Growth Des.*, 2001, **1**, 191–194.

21 D. A. Bashirov, T. S. Sukhikh, N. V. Kuratieva, D. Yu. Naumov, S. N. Konchenko, N. A. Semenov and A. V. Zibarev, *Polyhedron*, 2012, **42**, 168–174.

22 T. S. Sukhikh, D. S. Ogienko, D. A. Bashirov and S. N. Konchenkoa, *Russ. Chem. Bull*., 2019, **68**, 651–661.

23 Q. Cheng, X. Han, Y. Tong, C. Huang, J. Ding and H. Hou, *Inorg. Chem.*, 2017, **56**, 1696–1705.

24 W.-Q. Zhang, Q.-Y. Li, J.-Y. Cheng, K. Cheng, X. Yang, Y. Li, X. Zhao and X.-J. Wang, *ACS Appl. Mater. Interfaces*, 2017, **9**, 31352–31356.

25 R. J. Marshall, Y. Kalinovskyy, S. L. Griffin, C. Wilson, B. A. Blight and R. S. Forgan, *J. Am. Chem. Soc.*, 2017, **139**, 6253–6260.

26 D. Zhao, D. Yue, K. Jiang, Y. Cui, Q. Zhang, Y. Yang and G. Qian, *J. Mater. Chem. C*, 2017, **5**, 1607–1613.

27 W.-C. Song, L. Liang, X.-Z. Cui, X.-G. Wang, E.-C. Yang, X.-J. Zhao, *CrystEngComm*, 2018, **20**, 668–678.

28 T. Mocanu, N. Plyuta, T. Cauchy, M. Andruh and N. Avarvari, *Chemistry*, 2021, **3**, 269–287.

29 M. Andruh, *Chem. Commun.*, 2011, **47**, 3025–3042.

30 R. M. Clarke and T. Storr, *Dalton Trans.*, 2014, **43**, 9380–9391.

31 M. Andruh, *Dalton Trans.*, 2015, **44**, 16633–16653.

32 X. Song, H. Yu, X. Yan, Y. Zhang, Y. Miao, K. Ye and Y. Wang, *Dalton Trans.*, 2018, **47**, 6146–6155.

33 Y. Liu, Y. Lu, M. Prashad, O. Repič and T. J. Blacklock, *Adv. Synth. Catal.*, 2005, **347**, 217–219.

34 F. da Silva Miranda, A. M. Signori, J. Vicente, B. de Souza, J. P. Priebe, B. Szpoganicz, N. Sanches Gonçalves and A. Neves, *Tetrahedron*, 2008, **64**, 5410–5415.

35 A. V. Palii, D. V. Korchagin, E. A. Yureva, A. V. Akimov, E. Y. Misochko, G. V. Shilov, A. D. Talantsev, R. B. Morgunov, S. M. Aldoshin and B. S. Tsukerblat, *Inorg. Chem.*, 2016, **55**, 9696–9706.

36 T. J. Ozumerzifon, I. Bhowmick, W. C. Spaller, A. K. Rappé and M. P. Shores, *Chem. Commun.*, 2017, **53**, 4211–4214.

37 M. A. Palacios, J. Nehrkorn, E. A. Suturina, E. Ruiz, S. Gómez-Coca, K. Holldack, A. Schnegg, J. Krzystek, J. M. Moreno and E. Colacio, *Chem. Eur. J.*, 2017, **23**, 11649–11661.

38 A. A. Pavlov, Y. V. Nelyubina, S. V. Kats, L. V. Penkova, N. N. Efimov, A. O. Dmitrienko, A. V. Vologzhanina, A. S. Belov, Y. Z. Voloshin and V. V. Novikov, *J. Phys. Chem. Lett.*, 2016, **7**, 4111–4116.

39 L. Rigamonti, N. Bridonneau, G. Poneti, L. Tesi, L. Sorace, D. Pinkowicz, J. Jover, E. Ruiz, R. Sessoli and A. Cornia, *Chem. Eur. J.*, 2018, **24**, 8857–8868.

40 S. Tripathi, S. Vaidya, N. Ahmed, E. A. Klahn, H. Cao, L. Spillecke, C. Koo, S. Spachmann, R. Klingeler, G. Rajaraman, J. Overgaard and M. Shanmugam, *Cell Rep. Phys. Sci.*, 2021, **2**, 100404.

41 D. V. Korchagin, Y. E. Gureev, E. A. Yureva, G. V. Shilov, A. V. Akimov, E. Y. Misochko, R. B. Morgunov, K. V. Zakharov, A. N. Vasiliev, A. V. Palii, T. Lohmiller, K. Holldack and S. M. Aldoshin, *Dalton Trans.*, 2021, **50**, 13815–13822.

42 A. Świtlicka, B. Machura, J. Cano, F. Lloret and M. Julve, *ChemistrySelect*, 2021, **6**, 576–582.

43 J. Vallejo, I. Castro, R. Ruiz-García, J. Cano, M. Julve, F. Lloret, G. De Munno, W. Wernsdorfer and E. Pardo, *J. Am. Chem. Soc.*, 2012, **134**, 15704–15707.

44 D. Sadhukhan, P. Ghosh, C. J. Gómez-García and M. Rouzières, *Magnetochemistry*, 2018, **4**, 56.

45 A. Świtlicka, J. Palion-Gazda, B. Machura, J. Cano, F. Lloret and M. Julve, *Dalton Trans*., 2019, **48**, 1404–1417.

46 Y.-Y. Zhu, C. Cui, Y.-Q. Zhang, J.-H. Jia, X. Guo, C. Gao, K. Qian, S.-D. Jiang, B.-W. Wang, Z.-M. Wang and S. Gao, *Chem. Sci.*, 2013, **4**, 1802–1806.

47 V. V. Novikov, A. A. Pavlov, Y. V. Nelyubina, M.-E. Boulon, O. A. Varzatskii, Y. Z. Voloshin and R. E.P. Winpenny, *J. Am. Chem. Soc.*, 2015, **137**, 9792−9795.

48 Y.-Zhu Zhang, S. Gómez-Coca, A. J. Brown, M. R. Saber, X. Zhang and K. R. Dunbar, *Chem. Sci.*, 2016, **7**, 6519–6527.

49 A. Sarkar, S. Dey and G. Rajaraman, *Chem. Eur. J.*, 2020, **26**, 14036–14058.

50 Y. Peng, V. Mereacre, C. E. Anson, Y. Zhang, T. Bodenstein, K. Fink and A. K. Powell, *Inorg. Chem.*, 2017, **56**, 6056−6066.

51 D. Sertphon, K. S. Murray, W. Phonsri, J. Jover, E. Ruiz, S. G. Telfer, A. Alkaş, P. Harding and D. J. Harding, *Dalton Trans.*, 2018, **47**, 859–867.

52 S. Alvarez, *Chem. Rev.*, 2015, **115**, 13447–13483.

53 I. D. Brown and D. Altermatt, *Acta Crystallogr., Sect B*, 1985, **41**, 244–247.

54 R. M. Wood and G. J. Palenik, *Inorg. Chem.*, 1998, **37**, 4149–4151.

55 R. L. Carlin, *Magnetochemistry*, Springer-Verlag, Berlin, 1986, p 30.

56 F. Lloret, M. Julve, J. Cano, R. Ruiz-García and E. Pardo, *Inorg. Chim. Acta*, 2008, **361**, 3432–3445.

57 J. Cano, *VPMAG*, University of Valencia, Valencia, Spain, 2003.

58 G. De Munno, M. Julve, F. Lloret, J. Faus and A. Caneschi, *J. Chem. Soc., Dalton Trans.*, 1994, 1175–1183.

59 H. Sakiyama, R. Ito, H. Kumagai, K. Inoue, M. Sakamoto, Y. Nishida and M. Yamasaki, *Eur. J. Inorg. Chem.*, 2001, 2027–2032.

60 V. Mishra, F. Lloret and R. Mukherjee, *Inorg. Chim. Acta*, 2006, **359**, 4053–4062.

61 O. Fabelo, J. Pasán, F. Lloret, M. Julve and C. Ruiz-Pérez, *Inorg. Chem.*, 2008, **47**, 3568–3576.

62 A. Świtlicka-Olszewska, J. Palion-Gazda, T. Klemens, B. Machura, J. Vallejo, J. Cano, F. Lloret and M. Julve, *Dalton Trans.*, 2016, **45**, 10181–10193.

63 M. E. Lines, *Chem. Phys.*, 1971, **55**, 2977–2984.

64 J. Mayans, L. Tesi, M. Briganti, M.-E. Boulon, M. Font-Bardia, A. Escuer and L. Sorace, *Inorg. Chem.*, 2021, **60**, 8692–8703.

65 B. Cahier, R. Maurice, H. Bolvin, T. Mallah and N. Guihéry, *Magnetochemistry*, 2016, **2**, 31.

66 M. Viciano-Chumillas, G. Blondin, M. Clémancey, J. Krzystek, M. Ozerov, D. Armentano, A. Schnegg, T. Lohmiller, J. Telser, F. Lloret and J. Cano, *Chem. Eur. J.*, 2020, **26**, 14242–14251.

67 M. J. Frisch, G. W. Trucks, H. B. Schlegel, G. E. Scuseria, M. A. Robb, J. R. Cheeseman, G. Scalmani, V. Barone, B. Mennucci, G. A. Petersson, H. Nakatsuji, M. Caricato, X. Li, H. P. Hratchian, A. F. Izmaylov, J. Bloino, G. Zheng, J. L. Sonnenberg, M. Hada, M. Ehara, K. Toyota, R. Fukuda, J. Hasegawa, M. Ishida, T. Nakajima, Y. Honda, O. Kitao, H. Nakai, T. Vreven, J. A. Montgomery Jr., J. E. Peralta, F. Ogliaro, M. Bearpark, J. J. Heyd, E. Brothers, K. N. Kudin, V. N. Staroverov, R. Kobayashi, J. Normand, K. Raghavachari, A. Rendell, J. C. Burant, S. S. Iyengar, J. Tomasi, M. Cossi, N. Rega, J. M. Millam, M. Klene, J. E. Knox, J. B. Cross, V. Bakken, C. Adamo, J. Jaramillo, R. Gomperts, R. E. Stratmann, O. Yazyev, A. J. Austin, R. Cammi, C. Pomelli, J. W. Ochterski, R. L. Martin, K. Morokuma, V. G. Zakrzewski, G. A. Voth, P. Salvador, J. J. Dannenberg, S. Dapprich, A. D. Daniels, Ö. Farkas, J. B. Foresman, J. V Ortiz, J. Cioslowski, D. J. Fox, *Gaussian 09, Revision D.01*, Gaussian, Inc., Wallingford CT, 2009.

68 C. Adamo and V. Barone, *J. Chem. Phys*., 1999, **110**, 6158–6170.

69 A. Schäfer, H. Horn and R. Ahlrichs, *J. Chem. Phys.*, 1992, **97**, 2571–2577.

70 A. Schäfer, C. Huber and R. Ahlrichs, *J. Chem. Phys.*, 1994, **100**, 5829–5835.

71 J. Tomasi, B. Mennucci and R. Cammi, *Chem. Rev.*, 2005, **105**, 2999–3093.

72 A. D. Becke, *Phys. Rev. A*, 1998, **38**, 3098–3100.

73 C. Lee, W. Yang and R. G. Parr, *Phys. Rev. B*, 1988, **37**, 785–789.

74 A. D. Becke, *J. Chem. Phys.*, 1993, **98**, 5648–5652.

75 T. Yanai, D. P. Tew and N. C. Handy, *Chem. Phys. Lett.*, 2004, **393**, 51–57.

76 E. Ruiz, A. Rodríguez-Fortea, J. Cano, S. Alvarez and P. Alemany, *J. Comput. Chem.*, 2003**, 24**, 982–989.

77 E. Ruiz, J. Cano, S. Alvarez and P. Alemany, *J. Comput. Chem.*, 1999**, 20**, 1391–1400.

78 E. Ruiz, J. Cano, S. Alvarez and P. Alemany, *J. Am. Chem. Soc.*, 1998**, 120**, 11122–11129.

79 C. Angeli, R. Cimiraglia and J. P. Malrieu, *Chem. Phys. Lett.*, 2001, **350**, 297–305.

80 C. Angeli, R. Cimiraglia and J.-P. Malrieu, *J. Chem. Phys.*, 2002, **117**, 9138–9153.

81 C. Angeli, R. Cimiraglia, S. Evangelisti, T. Leininger and J.-P. Malrieu, *J. Chem. Phys.*, 2001, **114**, 10252–10264.

82 F. Neese, *Wires Comput. Mol. Sci.*, 2012, **2**, 73–78.

83 F. Weigend and R. Ahlrichs, *Phys. Chem. Chem. Phys.*, 2005, **7,** 3297–3305.

84 F. Weigend, *Phys. Chem. Chem. Phys.*, 2006, **8**, 1057–1065.

85 K. Eichkorn, O. Treutler, H. Ohm, M. Haser and R. Ahlrichs, *Chem. Phys. Lett*., 1995, **242**, 652–660.

86 K. Eichkorn, F. Weigend, O. Treutler, H. Ohm and R. Ahlrichs, *Theor. Chem. Acc*., 1997, **97**, 119–124.

87 F. Neese, F. Wennmohs, A. Hansen and U. Becker, *Chem. Phys.*, 2009, **356**, 98–109.

88 R. Izsák and F. Neese, *J. Chem. Phys.*, 2011, **135**, 144105.

89 R. Izsák, A. Hansen and F. Neese, *J. Chem. Phys.*, 2012, **110**, 2413–2417.

90 S. Stoll and A. Schweiger, *J. Magn. Reson.*, 2006, **178**, 42–55.